Schottky mass measurements of heavy neutron-rich nuclides in the element range $70 \leqslant Z \leqslant 79$ at the GSI Experimental Storage Ring

D. Shubina,[1,2,3] R. B. Cakirli,[1,4] Yu. A. Litvinov,[1,3] K. Blaum,[1] C. Brandau,[3,5] F. Bosch,[3] J. J. Carroll,[6] R. F. Casten,[7]
D. M. Cullen,[8] I. J. Cullen,[9] A. Y. Deo,[9] B. Detwiler,[10] C. Dimopoulou,[3] F. Farinon,[3] H. Geissel,[3,11] E. Haettner,[11] M. Heil,[3]
R. S. Kempley,[9] C. Kozhuharov,[3] R. Knöbel,[3] J. Kurcewicz,[3,20] N. Kuzminchuk,[11] S. A. Litvinov,[3] Z. Liu,[12,13] R. Mao,[13]
C. Nociforo,[3] F. Nolden,[3] Z. Patyk,[14] W. R. Plass,[11] A. Prochazka,[3] M. W. Reed,[9,15] M. S. Sanjari,[3,16] C. Scheidenberger,[3,11]
M. Steck,[3] Th. Stöhlker,[3,17,18] B. Sun,[11,19] T. P. D. Swan,[9] G. Trees,[10] P. M. Walker,[9,20] H. Weick,[3] N. Winckler,[1,3] M. Winkler,[3]
P. J. Woods,[12] T. Yamaguchi,[21] and C. Zhou[7]

[1]*Max-Planck-Institut für Kernphysik, Saupfercheckweg 1, 69117 Heidelberg, Germany*
[2]*Fakultät für Physik und Astronomie, Universität Heidelberg, Philosophenweg 12, 69120 Heidelberg, Germany*
[3]*GSI Helmholtzzentrum für Schwerionenforschung, Planckstraße 1, 64291 Darmstadt, Germany*
[4]*Department of Physics, University of Istanbul, Istanbul, Turkey*
[5]*ExtreMe Matter Institute EMMI, GSI Helmholtzzentrum für Schwerionenforschung, 64291 Darmstadt, Germany*
[6]*US Army Research Laboratory, 2800 Powder Mill Road, Adelphi, Maryland, USA*
[7]*Wright Nuclear Structure Laboratory, Yale University, New Haven, Connecticut 06520, USA*
[8]*Schuster Laboratory, University of Manchester, Manchester M13 9PL, United Kingdom*
[9]*Department of Physics, University of Surrey, Guildford, Surrey GU2 7XH, United Kingdom*
[10]*Youngstown State University, One University Plaza, Youngstown, Ohio 44555, USA*
[11]*II Physikalisches Institut, Justus-Liebig-Universität Gießen, 35392 Gießen, Germany*
[12]*School of Physics and Astronomy, University of Edinburgh, Edinburgh EH9 3JZ, United Kingdom*
[13]*Institute of Modern Physics, Chinese Academy of Sciences, Lanzhou 730000, People's Republic of China*
[14]*National Centre for Nuclear Research, PL-00681 Warsaw, Poland*
[15]*Department of Nuclear Physics, R.S.P.E., Australian National University, Canberra ACT 0200, Australia*
[16]*Goethe-Universität Frankfurt, 60438 Frankfurt, Germany*
[17]*Friedrich-Schiller-Universität Jena, 07737 Jena, Germany*
[18]*Helmholtz-Institut Jena, 07743 Jena, Germany*
[19]*School of Physics and Nuclear Energy Engineering, Beihang University, 100191 Beijing, People's Republic of China*
[20]*CERN, CH-1211 Geneva 23, Switzerland*
[21]*Graduate School of Science and Engineering, Saitama University, Saitama 338-8570, Japan*

Storage-ring mass spectrometry was applied to neutron-rich ^{197}Au projectile fragments. Masses of ^{181,183}Lu, ^{185,186}Hf, ^{187,188}Ta, ^{191}W, and ^{192,193}Re nuclei were measured for the first time. The uncertainty of previously known masses of ^{189,190}W and ^{195}Os nuclei was improved. Observed irregularities on the smooth two-neutron separation energies for Hf and W isotopes are linked to the collectivity phenomena in the corresponding nuclei.

I. INTRODUCTION

The binding energy of the nucleus, or its mass, contains information about interactions among its constituent protons and neutrons. Precision mass data as well as separation energies extracted from them can unveil much about the underlying nuclear structure [1,2]. For instance, magic numbers can easily be seen from separation energies which reveal a huge drop (depending on the size of the closed shell) or a jump or a gap (depending on the way the separation energy is constructed) after a magic number [3]. In addition, separation energies can reflect collective effects, as we will discuss below. Such data are therefore valuable in understanding the underlying shell structure in nuclei and the evolution of collective effects and are therefore essential to provide the basis for the development and testing of a comprehensive theory of nuclei. In turn, a reliable nuclear theory is of utmost importance for calculating the properties of unknown nuclei, which are needed, for

example, in the modeling of the rapid neutron capture process (r-process) of nucleosynthesis in stars [4]. Therefore, new data on neutron-rich heavy nuclei are essential.

However, such data are scarce mainly due to the complexity of producing these exotic nuclei. This becomes evident if one glances at the chart of nuclides (see, e.g., Ref. [5]), where for elements $Z \sim 70$–80 the number of observed neutron-rich nuclides is very limited. Very recently, several tens of new isotopes were discovered in projectile fragmentation of uranium beams, though no spectroscopic information could yet be obtained for these nuclei [6]. Their production rates are tiny, which requires very efficient measurement techniques. One such technique for mass measurements is storage-ring mass spectrometry [7].

In this paper we report on direct mass measurements of neutron-rich nuclei in the element range from lutetium to osmium. Masses for nine nuclei were measured for the first time, and for three nuclei the mass uncertainty was

improved. It is known that nuclear collective effects can be seen in the behavior of nucleon separation energies [8]. Here, we investigate the relation between rather subtle effects in two-neutron separation energies, S_{2n}, and changes in both collectivity and neutron number. Observed irregularities in the smooth two-neutron separation energies for Hf and W isotopes are linked to changes in collective observables. The importance of the number of valence nucleons is discussed in the context of collective contributions to binding energies calculated with the IBA model [9].

II. EXPERIMENT

The experiment was conducted at GSI Helmholtzzentrum für Schwerionenforschung in Darmstadt. Heavy neutron-rich nuclei of interest were produced in projectile fragmentation of ^{197}Au primary beams. The experiment described here was part of a larger experimental campaign, some results of which are described in Refs. [10–13]. The ^{197}Au beams were accelerated to an energy of 11.4 MeV/u in the linear accelerator UNILAC and then injected into the heavy-ion synchrotron SIS-18 [14], where they were further accelerated to an energy of 469.35 MeV/u. The ^{197}Au^{65+} beams were fast extracted (within about 1 μs) and focused on a production target located at the entrance of the fragment separator FRS [15,16]. As target we used 1036 mg/cm^2 thick ^{9}Be with a 221 mg/cm^2 Nb backing for more efficient electron stripping. The reaction products emerged from the target as highly charged ions having mostly 0, 1, or 2 bound electrons. The nuclides of interest were transported through the FRS, being operated as a pure magnetic rigidity ($B\rho$) analyzer [16], and injected into the cooler-storage ring ESR [17]. The transmission through the FRS and the injection into the ESR were optimized with the primary beam, and the magnetic setting of FRS-ESR was fixed at $B\rho = 7.9$ Tm throughout the entire experiment. All ion species within the acceptance of the FRS-ESR of about $\pm 0.2\%$ were injected and stored. Only 25% of the ESR acceptance is filled at the injection. We note that, in contrast to the settings described in Refs. [10,11], in this experiment no energy-loss degraders were employed in the FRS.

The relationship among relative revolution frequencies (f), relative mass-to-charge ratios (m/q), and velocities (v) of the particles stored in a ring is given by [7,18–20]

$$\frac{\Delta f}{f} = -\alpha_p \frac{\Delta \frac{m}{q}}{\frac{m}{q}} + (1 - \alpha_p \gamma^2) \frac{\Delta v}{v}, \qquad (1)$$

where γ is the relativistic Lorentz factor and α_p is the momentum compaction factor, which characterizes the relative variation of the orbit length of stored particles per relative variation of their magnetic rigidity (for more details see Refs. [7,18–20]). For the ESR, α_p is nearly constant for the entire revolution frequency acceptance and is $\alpha_p \approx 0.179$. From Eq. (1) it becomes obvious that the revolution frequency is a measure of the mass-to-charge ratios of the stored ions provided that the second term on the right-hand side, containing the velocity spread ($\Delta v/v$), can be eliminated. The latter is achieved by applying electron cooling [21]. For this purpose the stored ions are merged over a length of about 2.5 m

with a continuous beam of electrons in the electron-cooler device. The mean circumference of the ESR is 108.4 m and at our energies the ions circulate with a frequency of about 2 MHz, passing the electron cooler at each revolution. The energy of the electrons is very accurately defined by the applied acceleration potential. Within a few seconds the mean velocity of the ions becomes equal to the mean velocity of the electrons. The velocity spread of the stored ions, which is $\Delta v/v \approx 4 \times 10^{-3}$ at the injection, is thereby reduced to $\Delta v/v \approx 10^{-7}$ [21].

The Schottky mass spectrometry (SMS) technique has been applied to the electron-cooled ions [7,19]. In this technique, every stored highly charged ion at each revolution in the ESR induces mirror charges on a couple of parallel electrostatic copper plates, the Schottky pick-up installed inside the ring aperture. The noise from the pick-up, which is dominated by thermal noise, is amplified by a broad-band low-noise amplifier [22]. In the present experiment, we analyzed the noise power at about 60 MHz, corresponding to the 30th harmonic of the revolution frequency of the stored ions. The pick-up signal was down-mixed using a ∼60-MHz reference frequency from an external frequency generator. The acceptance of the ESR at the 30th harmonic corresponds to about 320 kHz [23,24]. Therefore, to cover the entire ESR acceptance we digitized the signal with a sampling frequency of 640 kHz using a commercial 16-bit analog-to-digital converter (ADC) [25]. A Fourier transform of the digitized data yielded the noise-power density spectrum, or the Schottky frequency spectrum [7,24].

New ions were injected every few minutes. At the injection into the ESR, the previously stored ions were removed. Several Schottky frequency spectra were created for each injection. The parameters of the Fourier transform algorithm were optimized offline. A frequency resolution of 4.77 Hz/channel was chosen; this corresponds to a time resolution of 0.21 s per spectrum. Furthermore, every 50 consecutive Schottky spectra were averaged to enhance the signal-to-noise ratio. Thus, Schottky spectra integrated over 10 s were produced. The latter means that several independent subsequent frequency spectra were obtained for each injection of the ions into the ESR.

The electron cooling forces the ions to the same mean velocity, thus filling the entire acceptance of the ESR of $\Delta B\rho/B\rho \sim \pm 1.5\%$ (see Ref. [19]). Since $B\rho = mv\gamma/q$, by changing the velocity of the electrons in different injections, ions with different m/q can be studied. In the present experiment we varied the electron-cooler voltage in the range from 204 to 218 kV. On average eight injections were recorded for each cooler setting. In order to facilitate the assignment of the revolution frequencies with the corresponding isotope identification, all spectra within each cooler setting were combined together. In this case the maximum number of ion species present in each setting can be used for the identification. The latter is done based on Eq. (1). As a starting point for the identification we used the frequency of the stored ^{197}Au^{76+} primary ions. An example of the combined Schottky frequency spectrum for an electron-cooler voltage of $U_c = 209$ kV is illustrated in Fig. 1. Figure 2 shows a zoom-in view on a quadruplet of lines of $A = 190$ isobars present in ground and/or isomeric states. The latter are indicated with
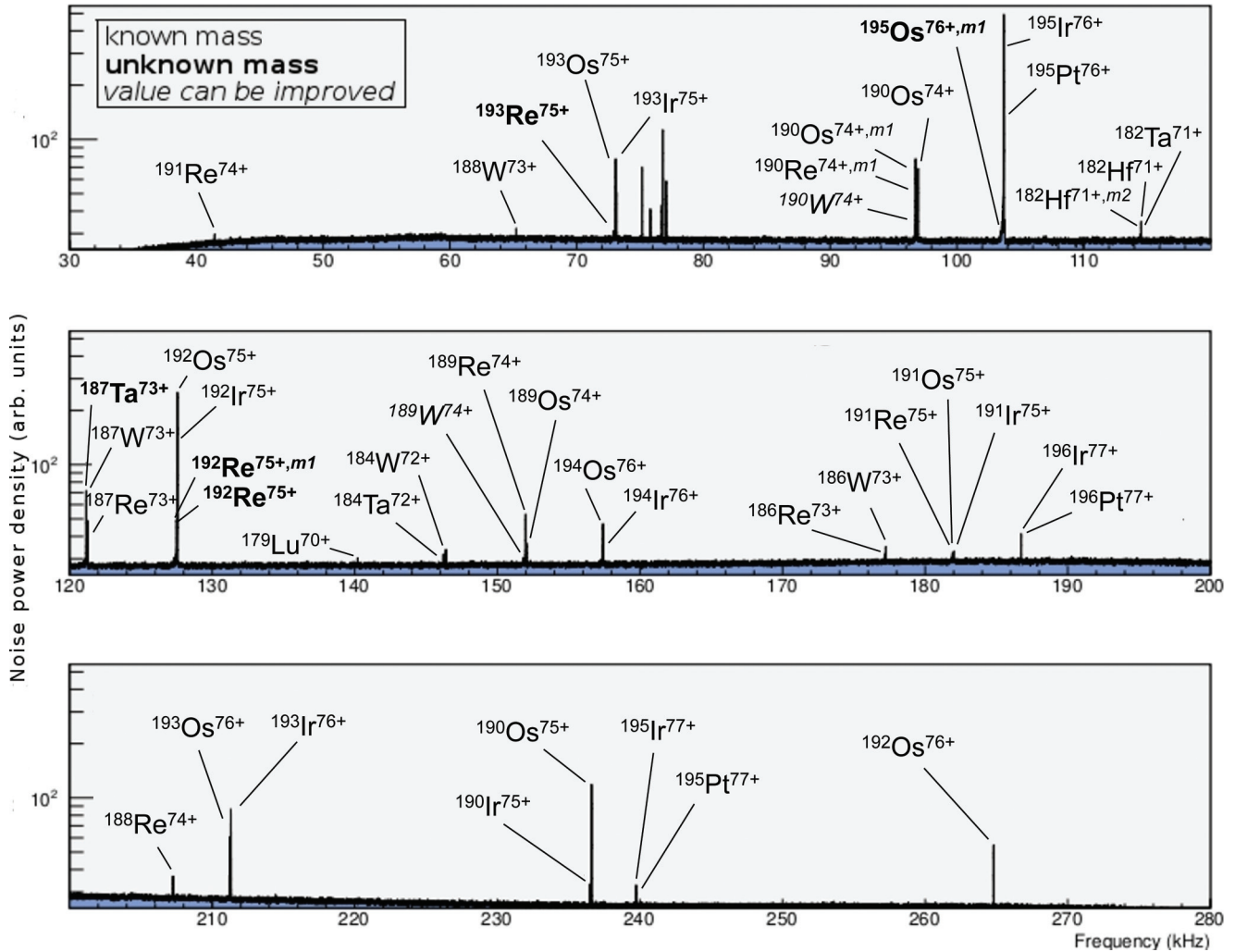
FIG. 1. (Color online) Example of a Schottky frequency spectrum with the corresponding isotope identification. This spectrum is combined from eight independent injections acquired for the electron-cooler voltage $U_c = 209$ kV. Nuclides with known and previously unknown masses are indicated by different fonts (see legend).

a label m. Peak finding and isotope identification were done automatically with dedicated ROOT-based [26] software [27]. The nuclides observed in this experiment are illustrated on the
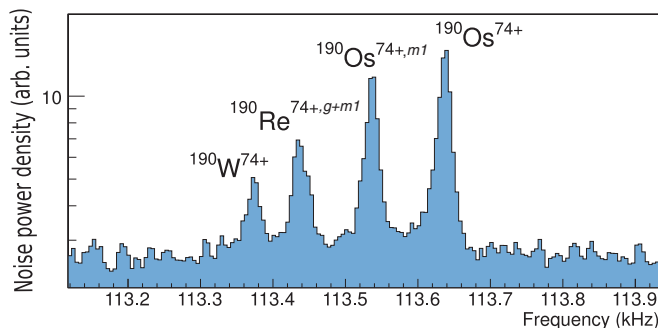

FIG. 2. (Color online) A zoomed-in view of the Schottky frequency spectrum illustrated in Fig. 1 on a quadruplet of $A = 190$ isobars. The peaks corresponding to nuclides in isomeric states are labeled with m.

chart of nuclides in Fig. 3 together with the nuclides in the ground and isomeric states identified in the other part of this experiment (see Refs. [10–13]).

III. DATA ANALYSIS AND RESULTS

In order to determine the unknown mass-to-charge ratios, the Schottky frequency spectra have to be calibrated [19,24]. For this purpose we selected the nuclides which were identified in our spectra and for which masses are known experimentally according to the Atomic Mass Evaluation (AME) 2003 [28]. We note that an update of the AME was made available in 2011 [29], which however contains no new information in the mass region studied here. The data of the present work were already included in the latest AME published very recently [30]. Furthermore, we required that the reference masses were obtained by more than one independent measurement technique and that there must exist no other ionic species with a close mass-to-charge ratio which could simultaneously be stored in the ESR. Also the peaks corresponding to
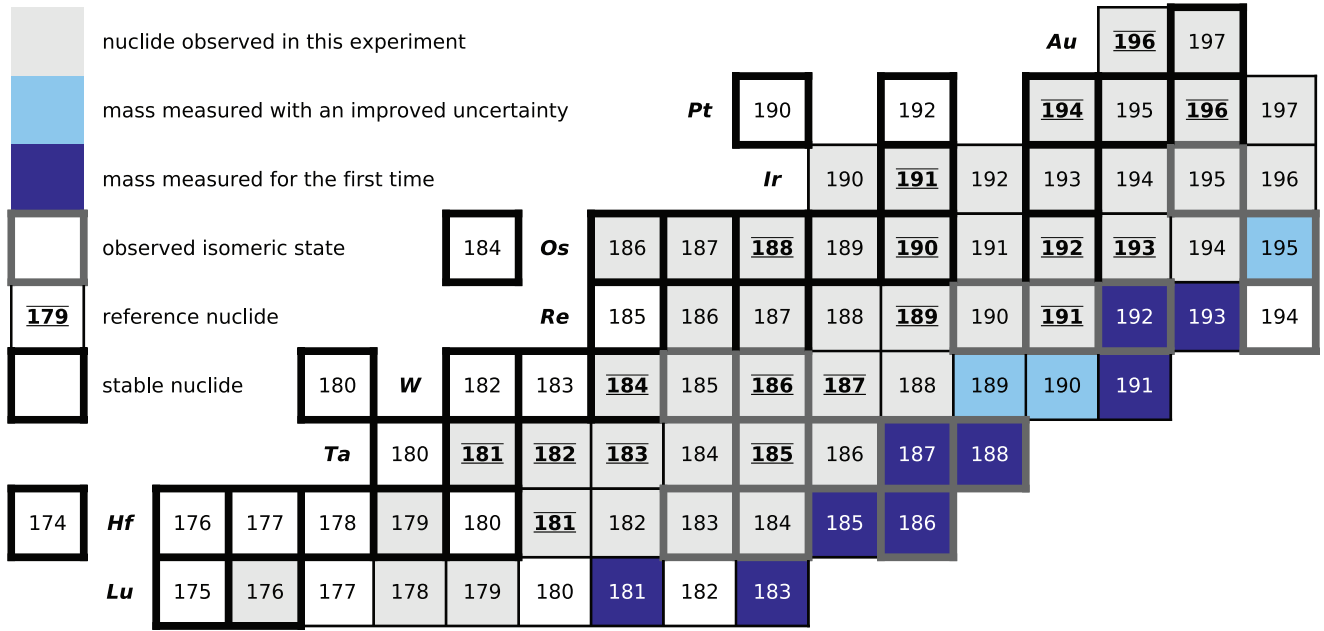
Legend (Fig. 3):
- nuclide observed in this experiment
- mass measured with an improved uncertainty
- mass measured for the first time
- observed isomeric state
- **179** reference nuclide
- stable nuclide

Chart of nuclides (Fig. 3):
- **Au**: 196, 197
- **Pt**: 190, 192, 194, 195, 196, 197
- **Ir**: 190, 191, 192, 193, 194, 195, 196
- **Os**: 184, 186, 187, 188, 189, 190, 191, 192, 193, 194, 195
- **Re**: 185, 186, 187, 188, 189, 190, 191, 192, 193, 194
- **W**: 180, 182, 183, 184, 185, 186, 187, 188, 189, 190, 191
- **Ta**: 180, 181, 182, 183, 184, 185, 186, 187, 188
- **Hf**: 174, 176, 177, 178, 179, 180, 181, 182, 183, 184, 185, 186
- **Lu**: 175, 176, 177, 178, 179, 180, 181, 182, 183

FIG. 3. (Color online) A part of the chart of nuclides indicating the nuclides measured in this work as well as the nuclides in the ground and isomeric states identified in the other part of this experiment devoted to the search for new K isomers in this region [10,11].

long-lived isomeric states (^{182}Hf^{m1}, ^{186}W^{m2}, ^{190}Os^{m1}, and ^{190}Ir^{m2} isomers) were not used for calibration. The list of reference masses is given in Table I.

TABLE I. Nuclides with accurately known masses used as references to calibrate Schottky frequency spectra. Listed are the proton (Z) and mass (A) numbers, the number of experimental settings (N_{set}) in which this reference mass was observed, literature mass excess values from the Atomic Mass Evaluation [28] (ME_{AME}), as well as the redetermined mass excess values (ME) (see text) with the corresponding σ_{stat} uncertainty and its difference from the literature value ($\delta = ME - ME_{AME}$). Note that the systematic uncertainty of $\sigma_{syst} = 38$ keV (see text) is not added here.

Z	A	N_{set}	ME_{AME} (keV)	ME (keV)	δ (keV)
72	181	1	−47412(2)	−47412(40)	0(40)
73	181	1	−48442(2)	−48383(40)	59(40)
73	182	3	−46433(2)	−46466(29)	−32(29)
73	183	3	−45296(2)	−45276(16)	20(16)
73	185	6	−41396(14)	−41350(14)	46(20)
74	184	5	−45707(1)	−45663(17)	44(17)
74	186	7	−42510(2)	−42493(12)	17(13)
74	187	8	−39905(2)	−39863(8)	41(8)
75	189	9	−37978(8)	−38063(10)	−85(13)
75	191	9	−34349(10)	−34364(3)	−15(11)
76	188	7	−41136(1)	−41115(12)	21(12)
76	190	7	−38706(2)	−38637(15)	69(15)
76	192	7	−35881(3)	−35833(8)	48(8)
76	193	7	−33393(3)	−33329(8)	63(8)
77	191	1	−36706(2)	−36650(71)	56(71)
78	194	4	−34763(1)	−34779(24)	−16(24)
78	196	9	−32647(1)	−32655(4)	−7(4)
79	196	5	−31140(3)	−31126(4)	14(5)

The momentum compaction factor α_p, although nearly constant, is a complicated function of the revolution frequency f. If α_p were exactly constant, then m/q would linearly depend on f. Figure 4 (top) shows an example of a linear fit through the calibration m/q values for one of the measured spectra. The residuals of the fit (bottom panel of the same figure) clearly show that the calibration function is more complicated than a low-order polynomial function. Polynomials of up to fourth order (with five free coefficients) were employed, but, in contrast to the analyses performed in Refs. [19,24,31], the quality of the fits was found unacceptable. A possible reason for the latter is the small number of reference masses
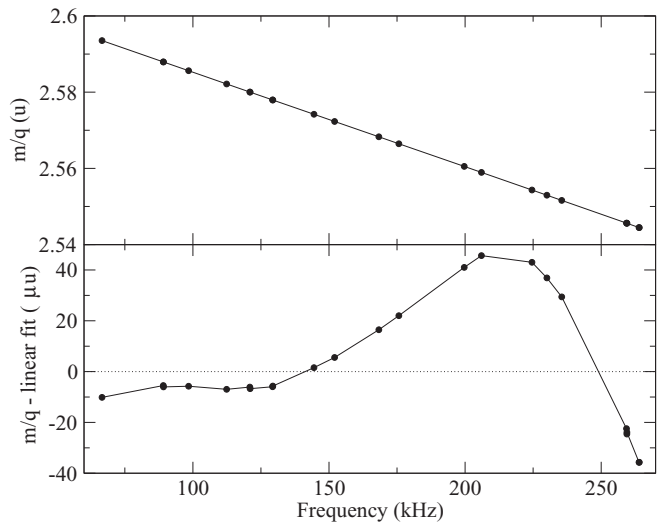
FIG. 4. Top: Mass-to-charge ratio m/q as a function of revolution frequency. The solid line illustrates a straight-line fit through the calibration m/q values. Bottom: The same as the top but with the linear fit subtracted.

TABLE II. Nuclides whose masses were determined for the first time (in boldface) or whose mass uncertainty was improved in this work. Listed are the proton (Z) and mass (A) numbers, the number of experimental settings (N_{set}) in which this nuclide was observed, and the obtained mass excess value (ME) with the corresponding 1σ total ($\sqrt{\sigma_{\text{stat}}^2 + \sigma_{\text{syst}}^2}$) uncertainty [$\sigma(ME)$].

Z	A	N_{set}	ME (keV)	$\sigma(ME)$ (keV)
71	**181**	**1**	**−44797**	**126**
71	**183**	**1**	**−39716**	**80**
72	**185**	**1**	**−38320**	**64**
72	**186**	**1**	**−36424**	**51**
73	**187**	**2**	**−36896**	**56**
73	**188**	**2**	**−33612**	**55**
74	189	5	−35618	40
74	190	7	−34388	41
74	**191**	**1**	**−31176**	**42**
75	**192**	**1**	**−31589**	**71**
75	**193**	**7**	**−30232**	**39**
76	195	1	−29512	56

in individual 10-s Schottky spectra. Furthermore, due to time variations of the storage ring and electron-cooler parameters, such as, e.g., their magnetic fields, it is not possible to establish a universal calibration curve. Therefore, we employed an analysis procedure in which we used linear splines to approximate the calibration curve in each individual spectrum.

Changes of the electron-cooler voltage were done in steps of 0.5 kV so that for adjacent cooler settings the measured frequency spectra have a significant overlap. Furthermore, the same nuclide can be present in different charge states, which allows for a redundant analysis. The nuclides whose masses have been measured for the first time or for which mass accuracy was improved in this work are listed in Table II.

Since the calibration curve is not known exactly and is approximated with linear splines, and since the number of calibration points in each spectrum is small, there is inevitably a systematic error introduced by the analysis method. Ways to estimate systematic uncertainty have been described in our previous works [19,24,31]. For this purpose in the present work, we redetermined the mass of each reference nuclide. This was done consecutively by setting each of the references as "no" reference and obtaining its mass from the remaining 17 references. The redetermined mass-excess values are listed in Table I along with their literature values [28]. The systematic error σ_{syst} has been obtained from solving the following equation:

$$\sum_{i=1}^{N_{\text{ref}}} \frac{\left(ME_{\text{AME}}^{(i)} - ME^{(i)}\right)^2}{\sigma_{\text{AME}(i)}^2 + \sigma_{(i)}^2 + \sigma_{\text{syst}}^2} = N_{\text{ref}}, \qquad (2)$$

where $N_{\text{ref}} = 18$ is the number of reference nuclides and $ME^{(i)}$ ($\sigma_{(i)}$) and $ME_{\text{AME}}^{(i)}$ ($\sigma_{\text{AME}(i)}$) are the recalculated and literature mass-excess values (statistical uncertainties) of the ith reference nuclide, respectively. The systematic uncertainty of the present analysis amounts to $\sigma_{\text{syst}} = 38$ keV. The final

uncertainties listed in Table II were obtained from a quadratic sum of the systematic and statistical uncertainties.

We note that in contrast to Ref. [31] we do not observe any significant systematic dependence of the recalculated mass values versus their proton number and correspondingly do not reduce the systematic errors. A dedicated study should be performed to investigate the origin of this inconsistency.

IV. DISCUSSION

The new masses allow us to obtain interesting information on nuclear structure. Figure 5 (left and middle) shows two-neutron separation energies (S_{2n}) as a function of neutron number for $Z = 66$–78 in the $A \sim 180$ region. Figure 5 (left) is for even proton numbers while Fig. 5 (middle) is for odd proton numbers. The new S_{2n} values, for ^{181,183}Lu, ^{185,186}Hf, ^{187,188}Ta, ^{191}W, and ^{192,193}Re, calculated from the masses measured in this study, are marked in red. For known masses whose values were improved in this experiment, ^{189,190}W and ^{195}Os, the literature S_{2n} values are marked in black.

By inspecting Fig. 5 (left), one can notice that in the S_{2n} values of the even-Z nuclei a flattening in Yb, Hf, and W is seen at almost the last neutron numbers experimentally known. The flattening in S_{2n}(W), using the improved W masses, is confirmed and S_{2n} at $N = 117$ continues with the same behavior. In contrast to Hf and W, the new S_{2n}(Os) point, which is a bit lower at $N = 119$ than in previous measurements, shows no flattening.

Figure 5 (middle) with the new measured masses does not show similar effects in S_{2n} as in Fig. 5 (left). However, there is a small change in slope (a more rapid fall-off) at $N = 110$ compared to the lower N trend in $S_{2n}(_{71}$Lu), $S_{2n}(_{73}$Ta), and $S_{2n}(_{75}$Re) [and we also see this drop for $_{72}$Hf and $_{74}$W in Fig. 5 (left)] and maybe at $N = 115$ in $S_{2n}(_{73}$Ta) as well. It is highly desirable to have more odd-Z mass measurements in this region for a comparison with even-Z nuclei where more data are available. Thus, we concentrate below on discussing even-Z nuclei.

Figure 5 (right) shows the energy of the first excited 2^+ states against neutron number for $Z = 70$–78 in the $A \sim 180$ region. This important, simple observable has a high energy (up to a few MeV) at magic numbers where nuclei are spherical and very low energies (less than 100 keV for well-deformed heavy nuclei) near mid-shell. The $E(2_1^+)$ values usually decrease smoothly between the beginning and middle of a shell except when there is a sudden change in structure. Since $N \sim 104$ is mid-shell for the nuclei illustrated in Fig. 5, $E(2_1^+)$ has a minimum at or close to $N = 104$. After the mid-shell, the energy increases toward the $N = 126$ magic number.

Let us now focus on the W–Pt nuclei in Fig. 5 and compare the behavior of $E(2_1^+)$ and S_{2n}. In particular, we look at S_{2n} in isotopes where $E(2_1^+)$ changes rapidly, indicating a sudden change in structure. In W, $E(2_1^+)$ increases from $N = 114$ to 116 by a considerably larger amount compared to the other W isotopes (see Ref. [33]). This jump signals a structural change from approximately constant deformation to decreasing deformation at $N = 116$ (after $N = 114$). Note that this neutron number is exactly where S_{2n} exhibits flattening.
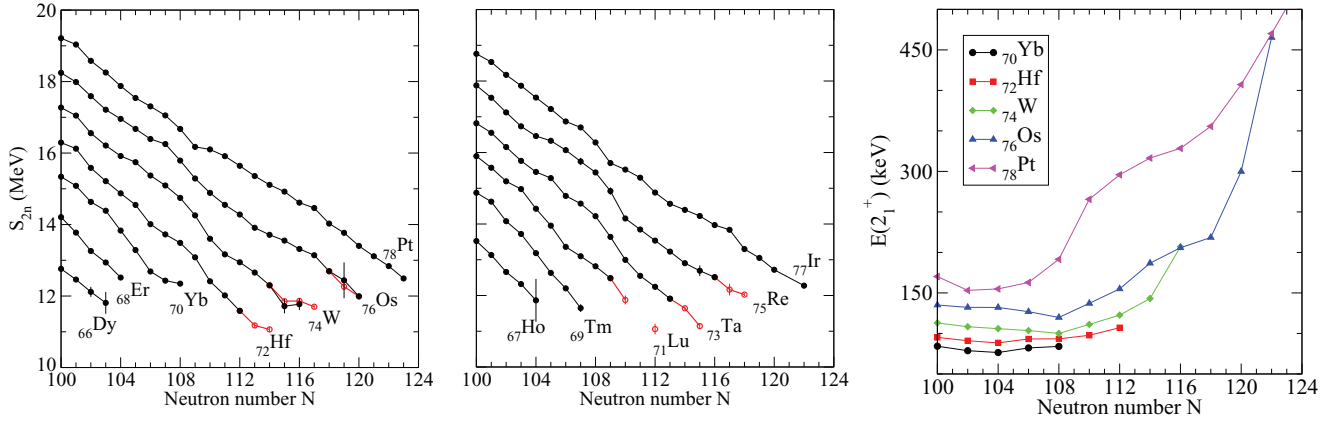
FIG. 5. (Color online) Data for the $A \sim 180$ region, two-neutron separation energies [28] as a function of neutron number from $N = 100$ to $N = 124$ for even Z (left) from Dy to Pt and odd Z (middle) from Ho to Re. The new S_{2n} values obtained from this work are shown in red while the literature S_{2n} values are shown in black. Right: Energies of the first excited 2^+ states [32] for the same even-even nuclei as in the left panel.

Similar to W, Os at $N = 120$ (after $N = 118$) has a jump in $E(2_1^+)$. However, $S_{2n}(^{196}\text{Os})$ does not reveal an obvious change at the same neutron number. At first glance, this seems inconsistent with the interpretation explained for W above but, in fact, there might be an explanation for this different behavior which would provide additional insight into the relation of binding to collectivity.

In Ref. [8] the structural sensitivity of calculated collective contributions to binding was shown. In addition the authors of Ref. [8] stressed that collective binding is very sensitive to the number of valence nucleons. Calculated collective contributions to binding using the IBA-1 model for boson numbers $N_B = 5$ (left) and $N_B = 16$ (right) are illustrated in the symmetry triangle [8] in Fig. 6. The three corners of the triangle describe three dynamical symmetries: U(5) (vibrator), SU(3) (rotor), and O(6) (γ-soft) (for more details, see Ref. [9]). The color code in Fig. 6 changes from yellow to red when the collective effects increase. Needless to say, nuclei have more valence particles (so boson numbers) around the SU(3) corner than the U(5) [and also O(6)] corner. One sees that the collective binding energy rapidly increases for nuclei with

axial deformation, that is, near SU(3). Note that the triangles are presented for fixed boson numbers. In both, the color scale is kept the same to point out that the collective binding energies are larger in $N_B = 16$ than in $N_B = 5$. As shown in Fig. 4 of Ref. [8], the collective binding energies vary approximately as the square of the number of valence nucleons in the context of IBA calculations. Therefore, for a lower number of valence nucleons, Fig. 6 shows similar trends for both $N_B = 5$ and $N_B = 16$, but the overall binding is considerably less [compare (left) and (right) of Fig. 6]. We now suggest that the behavior of $E(2_1^+)$ and S_{2n} in Fig. 5 can be understood in terms of this dual dependence of binding on collectivity and valence nucleon number.

If ^{190}W and ^{196}Os are mapped in the symmetry triangle, ^{190}W will likely be closer to the SU(3) corner than ^{196}Os [34]. One of the ways to understand this is from the P factor [35], defined as $P = N_p N_n / (N_p + N_n)$, where N_p denotes the number of valence protons (proton holes) and N_n the number of valence neutrons (neutron holes). Thus P is a quantity that can provide a guide to structure. For example, the onset of deformation in heavy nuclei corresponds to the P factor around 4 and 5. Generally, if P is larger than 3, collective effects increase. That is, nuclei become deformed and approach closer to the SU(3) corner.

Figure 7 shows color-coded values for the P factor for the $Z = 50$–82, $N = 82$–126 region and indicates the P factors for the nuclei relevant to this discussion. ^{190}W has 8 valence protons and 10 valence neutrons while ^{196}Os has $N_p = 6$ and $N_n = 6$. Correspondingly, these nuclei have P factors of 4.4 and 3, respectively. The greater collectivity of ^{190}W compared to ^{196}Os suggested by their P factors is reflected in its lower 2_1^+ energies as seen in Fig. 5 (right). Thus, for two reasons—both greater collectivity and more valence nucleons—the collective binding should be much greater in ^{190}W than in ^{196}Os and changes in binding energies ($S_{2n\text{-coll}}$ values) should be on a larger scale. We suggest that this accounts for the fact that we see a flattening in ^{190}W clearly but not in ^{196}Os in Fig. 5 (left). Obviously, it is very important to have new data (both
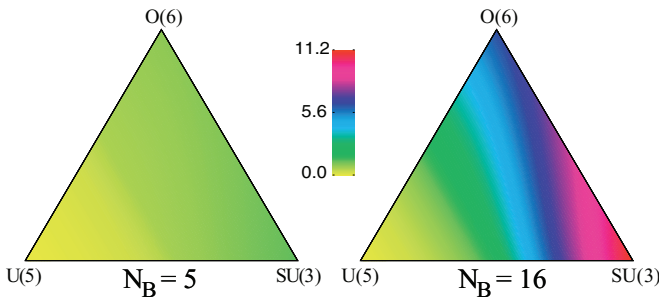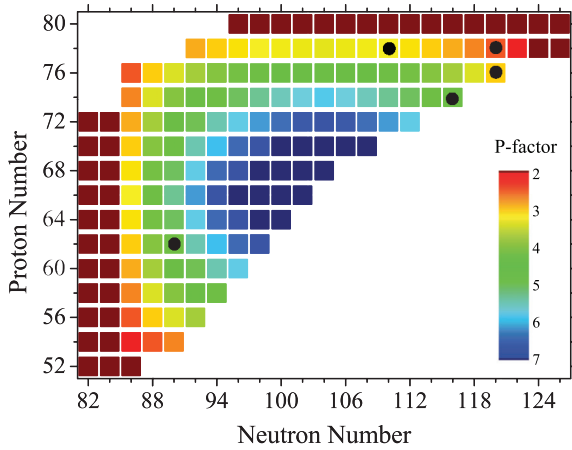

FIG. 6. (Color online) The symmetry triangle of the IBA showing the three dynamical symmetries at the vertices. The colors indicate calculated collective contributions in MeV to binding energies for $N_B = 5$ (left) and $N_B = 16$ (right). A similar triangle for $N_B = 16$ was presented in Ref. [8].

FIG. 7. (Color online) P-factor values illustrated with a color code for even-even nuclei in the $Z = 50$–82 and $N = 82$–126 shells. Black points marked are for the key nuclei discussed, namely, ^{190}W, ^{196}Os, ^{188}Pt, ^{198}Pt, and ^{152}Sm.

masses and spectroscopic information) on even more neutron rich W isotopes although such experiments are difficult. Even the mass of ^{192}W alone would be telling since the trend in $E(2_1^+)$ is quite clear already.

Existing data on Pt nicely illustrate and support these ideas. Figure 5 (right) shows two jumps in $E(2_1^+)$ for Pt, around $N \sim 110$ and $N \sim 118$–120. Looking at S_{2n} for Pt, one sees a kink near $N \sim 110$ but a smooth behavior near $N \sim 118$. For ^{188}Pt, N_p is 4 and N_n is 16 so the P factor is 3.2. This isotope, with 20 valence nucleons, is relatively collective and once again one sees an anomaly in S_{2n} as well. In contrast, for ^{198}Pt$_{120}$ with only 10 valence nucleons, and a P factor of only 2.4, the lower collectivity (seen in the much higher 2^+ energy) and the lower number of valence nucleons are such that S_{2n} shows no anomaly, but rather a nearly straight behavior.

This qualitative interpretation is supported by collective model calculations. A thorough and detailed study of this or any transition region requires a very careful and systematic assessment of all the data on energies, transition rates, and binding energies, the choice for the specific terms to include in the Hamiltonian, and the optimum approach to fitting the data. We are undertaking such a study and will present the results in a future publication. Nevertheless, it is useful to present an example of the model results here to validate the ideas presented above. To this end, we have carried out a schematic set of IBA calculations using the Hamiltonian [36,37]

$$H = \epsilon \hat{n}_d - \kappa Q \cdot Q \tag{3}$$

where Q is a quadrupolar operator

$$Q = (s^\dagger \tilde{d} + d^\dagger s) + \chi (d^\dagger \tilde{d})^{(2)}. \tag{4}$$

The first term in Eq. (3) drives nuclei spherical while the $Q \cdot Q$ term induces collectivity and deformation. Therefore a spherical-deformed transition region involves a systematic change in the ratio of ϵ to κ. No generality is lost by keeping κ constant (at 0.02 MeV). We follow a trajectory along the bottom axis of the triangle corresponding to $\chi = -1.3228$. Figure 8 illustrates the results, for $N_B = 6$–16, showing
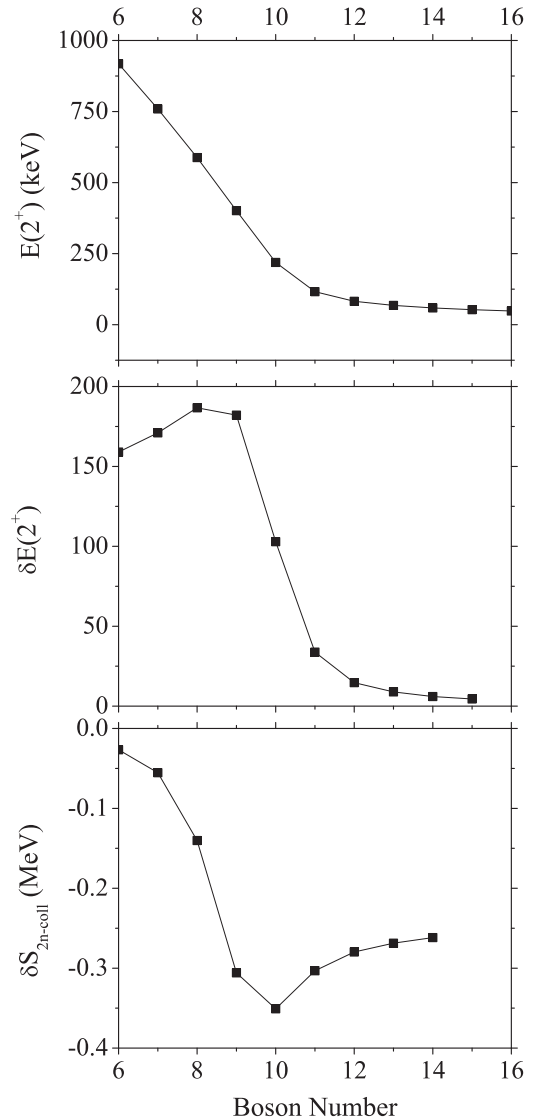

FIG. 8. Calculated $E(2_1^+)$ (top), $\delta E(2_1^+)$ (middle), and $\delta S_{2n\text{-coll}}$ (bottom) values from IBA calculations as a function of boson number N_B. The points for $\delta E(2_1^+)$ and $\delta S_{2n\text{-coll}}$ correspond to a set of schematic IBA calculations in which κ, and χ are constant (at 0.02 and -1.32, respectively) while ϵ and N_B vary in a smooth way to simulate a spherical-to-deformed transition region. The following equations are used for $\delta E(2_1^+)$ and $\delta S_{2n\text{-coll}}$: $\delta E(2_1^+)(Z, N) = [E(2_1^+)(Z, N) - E(2_1^+)(Z, N + 2)]/E(2_1^+)(Z, N)$ and $\delta S_{2n\text{-coll}} = -[S_{2n\text{-coll}}(Z, N) - S_{2n\text{-coll}}(Z, N + 2)]$, respectively.

$E(2_1^+)$ and the differentials of $E(2_1^+)$ (for $N_B = 6$–15) and for the collective contributions to S_{2n}, $S_{2n\text{-coll}}$ (for $N_B = 6$–14). There is a clear change in structure at $N_B \sim 10$ which is seen in a change in trend of $E(2_1^+)$. Between $N_B = 10$ and 11, $R_{4/2}$ changes from 2.60 to 3.13. This corresponds to a maximum in the normalized differential of $E(2_1^+)$. Confirming our association of structural changes with kinks in S_{2n}, the differential of the collective part of S_{2n} also shows an extremum at exactly the same point.

Besides the experimental examples of a correlation of $E(2_1^+)$ energies and S_{2n} values discussed in the context of Fig. 5, our interpretation can easily be illustrated with the Sm
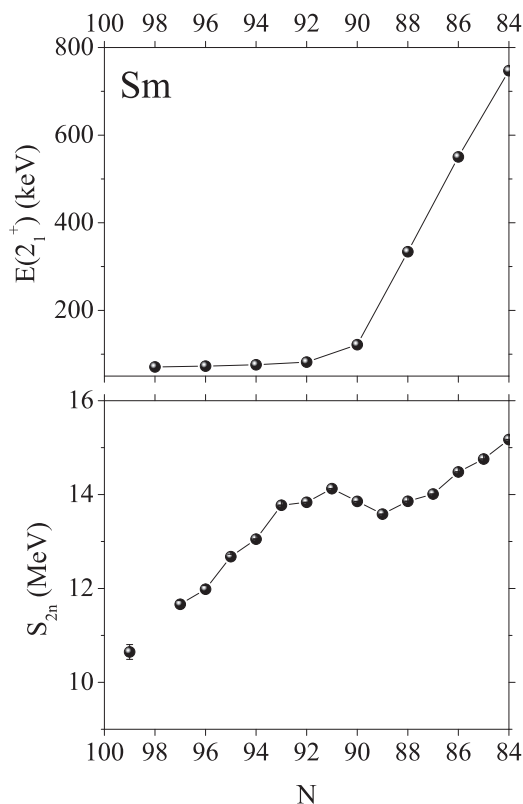
FIG. 9. Experimental $E(2_1^+)$ (top) and S_{2n} (bottom) values vs neutron number for $_{62}$Sm [29,32].

isotopes around $N = 90$. As is well known, there is a sudden onset of deformation for the rare earth nuclei from $N = 88$ to 90. This effect is clear from various observables. One example is seen in Fig. 9, which shows the experimental $E(2_1^+)$ energies (top) and S_{2n} (bottom) as a function of neutron number. Note that we plot these against decreasing neutron number so that the deformed nuclei are on the left and spherical ones on the right to make the comparison with Fig. 5 easier. Note also that the overall trend in S_{2n} is opposite from that in Fig. 5 since S_{2n} values decrease with increasing neutron number [going to the left in Fig. 9 (bottom)], which simply reflects the filling of the shell model orbits. The noticeable deviation occurs near $N \sim 90$, where there is a distinct flattening. To correlate the trends in these two observables in the $N = 90$ region, one can use the same interpretation as above for W at $N = 116$; namely, if there is a visible change at neutron number N in $E(2_1^+)$ and there are many valence nucleons, we expect to see a change in the behavior of S_{2n}. In Fig. 9 (top), the $E(2_1^+)$ change occurs at $N \sim 90$. The isotope ^{62}Sm at $N = 90$ has $N_p = 12$ and $N_n = 8$ so it has 10 bosons and its P factor is 4.8 (see Fig. 7). One therefore expects to see a change in S_{2n}. Figure 9 (bottom) confirms this expectation. The clear structural change at $N = 90$ shown in $E(2_1^+)$ is correlated with a larger binding compared to the general trend in S_{2n} as a function of N.

Similar correlations can be seen in some other nuclei as well. However, here, it is worth mentioning two more examples marked in Fig. 5. The case of Yb isotopes is interesting. Yb at $N = 107$ starts to change slope in S_{2n} and a flattening occurs at $N = 108$. The P factor is ~ 7. With the interpretation

above, one would expect to see a change in $E(2_1^+)$ after $N = 106$, at $N = 108$. However, there is no sudden change in $E(2_1^+)$ in ^{178}Yb. To understand Yb around $N \sim 108$ better, it might therefore be useful to have additional S_{2n} values (mass measurements) and also more spectroscopic results for the neutron-rich Yb isotopes.

Hf at $N = 114$ has a P factor 5.4 and one sees a flattening in S_{2n}. The corresponding 2^+ energies, however, are not known. Thus, similarly as in Yb, we need more spectroscopic results for Hf.

To summarize, we observed a correlation between the behavior of S_{2n} obtained from our measured masses with the spectroscopic data for $E(2_1^+)$, which could be related to nuclear collectivity and valence nucleon number.

V. CONCLUSION

Direct mass measurements of neutron-rich ^{197}Au projectile fragments at the cooler-storage ring ESR yielded new mass data. Masses of nine nuclides were obtained for the first time and for three nuclei the mass uncertainty was improved.

With the new masses, two-neutron separation energies, S_{2n}, are investigated. We showed that changes in structure, as indicated by changes in the collective observable $E(2_1^+)$, are reflected in S_{2n} values in nuclei such as ^{190}W and ^{188}Pt, which have large P factors, are collective, and have large valence nucleon numbers. For nuclei with similar changes in $E(2_1^+)$, such as ^{196}Os, and ^{198}Pt, which have lower collectivity and P factors, and fewer valence nucleons, the sensitivity of collective binding to structure is greatly reduced and smooth trends in S_{2n} are observed. In Hf, there are new S_{2n} values at $N = 113$, 114 where we see a flattening but there is no spectroscopic data at $N = 114$. To confirm the ideas discussed in this paper, it would be useful to measure $E(2_1^+)$ for Hf at $N = 114$. Similarly, mass and spectroscopic measurements are suggested for nuclei such as Yb with $N \sim 108$. To conclude, these new data illustrate subtle changes in structure and the correlation with $E(2_1^+)$ reveals a valuable way to correlate changes in structure in terms of both masses and spectroscopic observables. Of course, to quantitatively test these ideas requires a systematic collective model study of the mass-structure relationship in this region. Such a project has been initiated and we illustrated some of the results here.

[1] K. Blaum, Phys. Rep. **425**, 1 (2006).
[2] K. Blaum *et al*., J. Phys. Conf. Ser. **312**, 092001 (2011).
[3] Yu. N. Novikov *et al*., Nucl. Phys. A **697**, 92 (2002).
[4] C. A. Bertulani and A. Gade, Phys. Rep. **485**, 195 (2010).
[5] Chart of Nuclides, http://www.nndc.bnl.gov/chart.
[6] J. Kurcewicz *et al*., Phys. Lett. B **717**, 371 (2012).
[7] B. Franzke, H. Geissel, and G. Münzenberg, Mass Spectrom. Rev. **27**, 428 (2008).
[8] R. B. Cakirli, R. F. Casten, R. Winkler, K. Blaum, and M. Kowalska, Phys. Rev. Lett. **102**, 082501 (2009).
[9] F. Iachello and A. Arima, *The Interacting Boson Model* (Cambridge University Press, Cambridge, England, 1987).
[10] M. W. Reed *et al*., Phys. Rev. Lett. **105**, 172501 (2010).
[11] M. W. Reed, Doctoral thesis, University of Surrey, Guildford, 2012.
[12] M. W. Reed *et al*., J. Phys. Conf. Ser. **381**, 012058 (2012).
[13] M. W. Reed *et al*., Phys. Rev. C **86**, 054321 (2012).
[14] K. Blasche, D. Böhne, B. Franzke, and H. Prange, IEEE Trans. Nucl. Sci. **32**, 2657 (1985).
[15] P. Armbruster *et al*., AIP Conf. Proc. **164**, 839 (1987).
[16] H. Geissel *et al*., Nucl. Instrum Methods B **70**, 286 (1992).
[17] B. Franzke, Nucl. Instrum Methods B **24/25**, 18 (1987).
[18] T. Radon *et al*., Phys. Rev. Lett. **78**, 4701 (1997).
[19] T. Radon *et al*., Nucl. Phys. A **677**, 75 (2000).
[20] Yu. A. Litvinov and F. Bosch, Rep. Prog. Phys. **74**, 016301 (2011).
[21] M. Steck *et al*., Nucl. Instrum. Methods A **532**, 357 (2004).
[22] U. Schaaf, Doctoral thesis, Universität Frankfurt, 1991; GSI-Report 91-22, 1991.
[23] Yu. A. Litvinov *et al*., Nucl. Phys. A **734**, 473 (2004).
[24] Yu. A. Litvinov *et al*., Nucl. Phys. A **756**, 3 (2005).
[25] E. Kaza, Doctoral thesis, Giessen University, 2004.
[26] ROOT data analysis package, http://root.cern.ch/drupal/.
[27] D. Shubina, Doctoral thesis, Heidelberg University, 2012.
[28] A. H. Wapstra, G. Audi, and C. Thibault, Nucl. Phys. A **729**, 129 (2003).
[29] G. Audi *et al*., http://amdc.in2p3.fr/masstables/Ame2011int/filel.html.
[30] G. Audi *et al*., Chin. Phys. C **36**, 1287 (2012).
[31] L. Chen *et al*., Nucl. Phys. A **882**, 71 (2012).
[32] National Nuclear Data Center, http://www.nndc.bnl.gov/.
[33] Zs. Podolyak *et al*., Phys. Lett. B **491**, 225 (2000).
[34] R. B. Cakirli (private communication).
[35] R. F. Casten, D. S. Brenner, and P. E. Haustein, Phys. Rev. Lett. **58**, 658 (1987).
[36] D. D. Warner and R. F. Casten, Phys. Rev. Lett. **48**, 1385 (1982).
[37] P. O. Lipas, P. Toivonen, and D. D. Warner, Phys. Lett. B **155**, 295 (1985).